Second law analysis and optimization of a parabolic trough receiver tube for direct steam generation

H.C. Nolte[a] , T. Bello-Ochende[b,1], J.P. Meyer[a]

[a] *Department of Mechanical and Aeronautical Engineering, University of Pretoria, Private Bag X20, Hatfield, 0028, South Africa*

[b] *Department of Mechanical Engineering, University of Cape Town, Private Bag X3, Rondebosch, 7701, South Africa*

[1] Corresponding author: Tel: +27 21 650 3673 , Fax: +27 21 650 3240
Email addresses: henriettenolte@yahoo.com (H.C. Nolte), tunde.bello-ochende@uct.ac.za (T. Bello-Ochende), josua.meyer@up.ac.za (J.P. Meyer)

Abstract

Entropy generation in the receiver tube of a parabolic trough solar collector can mainly be attributed to the fluid friction and finite temperature differences. The contribution of each of these components is investigated under different circumstances. Mass flow rates, tube diameters and operating pressures are investigated to obtain good guidelines for receiver tube and plant design. Operating pressures between 3 MPa (saturation temperature of 233.9 °C) and 9 MPa (saturation temperature of 303.3 °C) were investigated.Results show that small diameters can result in excessive fluid friction, especially when the mass flow rates are high. For most cases, tube diameters beyond 20 mm will exclusively be subject to entropy generation due to finite temperature differences, and entropy generation due to fluid friction will be small to negligible. Increasing the concentration ratio will decrease entropy generation, due to a higher heat flux per unit meter. This will ultimately result in shorter receiver tube lengths. From a simulated annealing (SA) optimization it was seen that if the diameter is increased, the entropy generation can be lowered, provided that the concentration ratio is kept constant. However, beyond a certain point gains in minimizing the entropy generation become negligible. The optimal operating pressure will generally increase if the mass flow rate is increased. Finally it was seen that higher operating pressures are more advantageous when the entropy generation minimization is considered in conjunction with the work output.

Keywords:

parabolic trough receiver; direct steam generation; entropy generation minimization; optimization; small scale application

Nomenclature

A	Area (m^2)
A_s	Tube exposed heat transfer area (m^2)
C_R	Concentration ratio
D	Diameter (m)
E	Exergy (W)
f	Friction factor
$\dot{G}$	Mass velocity (kg/m^2s)
h	Heat transfer coefficient ($W/(m^2.K)$)
I_b	Solar beam radiation (W/m^2)
k	Thermal conductivity (W/(m.K))
L	Length (m)
$\dot{m}$	Mass flow rate (kg/s)
Nu	Nusselt number
P	Pressure (Pa)
Pr	Prandtl number
Q	Heat (W)
Re	Reynolds number
S_{gen}	Total entropy generation (W/K)
$S_{gen,dT}$	Entropy generation due to finite temperature differences (W/K)
$S_{gen,dP}$	Entropy generation due to fluid friction (W/K)
S_r	Reflected solar energy (W/m^2)

T	Temperature (℃ or K)
V	Velocity (m/s)
W_a	Aperture area (m)
x	Quality (% or fraction)

Greek symbols

ε	Emissivity
ε_{void}	Void fraction
η_{opt}	Optical efficiency (%)
μ	Dynamic viscosity (kg/m.s)
ν	Local specific volume (m^3/kg)
ρ	Density (kg/m^3)
σ	Stefan-Boltzmann constant (W/(m^2.K^4))
Φ^2	Two-phase flow multiplier

Subscripts

amb	Ambient
cb	Convective boiling
$cond$	Conduction
$conv$	Convection
des	Destroyed
$fluid$	Working fluid
G	Vapour
g	Glass
gi	Glass inner
go	Glass outer
in	Inlet
L	Liquid
nb	Nucleate boiling
out	Outlet
r	Receiver
rad	Radiation
ri	Receiver inner
ro	Receiver outer
sky	Effective sky
sun	Apparent sun
tp	Two-phase
$wind$	Wind

1. Introduction

Numerous experimental and comparative investigations have been made concerning parabolic trough technology [1-3]. Parabolic trough technology can use water as a working fluid. If water is used, only one cycle is incorporated and the superheated steam is eventually passed through a turbine to produce work. The process of heating liquid water to superheated steam in the receiver is also known as direct steam generation or DSG [1]. Odeh et al. [4] investigated the thermal performance of a parabolic trough collector by developing an

efficiency equation in terms of the receiver wall temperature rather than the fluid bulk mean temperature. This was done so that the model could be used for different working fluids. Forristall [5] implemented a heat transfer model into Engineering Equation Solver (EES) to investigate the performance of a parabolic trough receiver. Roesle et al. [6] numerically investigated the heat loss from a parabolic trough receiver tube with an active vacuum system by using computational fluid dynamics (CFD) and Monte Carlo ray tracing software. However, a second law analysis was not conducted in these models.

Koroneos et al. [7] conducted an exergy analysis of solar, wind as well as geothermal energy. Their research showed that the exergy lost in the receiver-collector subsystem is highest due to greater quality losses compared with the heat engine subsystem. The same conclusions were drawn by Singh et al. [8]. They concluded that the condenser component as well as the receiver component is responsible for the major exergy destruction where the receiver losses are of high quality. Since the exergy losses in the receiver component is of high quality the process of DSG in the receiver is the focus of this work. Entropy generation in the receiver tube can be attributed to fluid friction ($S_{gen,dP}$) as well as finite temperature differences ($S_{gen,dT}$) [9]. Ratts et al [10] used entropy generation minimisation to obtain an optimal Reynolds number for turbulent flow, as well as laminar flow. The investigation was extended for non-circular ducts. Sahin [11] explored entropy generation in a smooth duct subject to a constant wall temperature in the turbulent regime. Furthermore, the validity of a constant viscosity assumption was investigated and it was found to be valid for water when the viscosity variations are small. Revellin et al [12] investigated the local entropy generation for two-phase flow by considering a separated flow model as well as a mixture model. The study also investigates the effect of heat transfer enhancement and found that heat transfer enhancement can be beneficial at low mass velocities but not necessarily at high mass velocities. Often when attempting to minimize the entropy generation in a tube, conditions that would minimise the fluid friction component will increase the temperature difference (heat loss) component, therefore it is of importance to identify design guidelines that will result in optimality.

Parabolic trough technology incorporating DSG can reach temperatures up to 400℃ and pressures up to10 MPa [1,13]. Operating temperatures are not as high as for 3D focussing collectors, but can be well above ambient. At temperatures significantly higher than ambient, the receiver will be subject to large heat losses. Uneven heating or stratified flow can cause bending of the receiver tube. This can be detrimental, since bending can lead to breakage of the glass cover. The vacuum covering is very effective in retaining the heat, provided that it is maintained correctly.

In this research a second law analysis is used to optimise the receiver tube. To conduct the second law analysis a first law analysis is performed to solve the fluid temperature, receiver temperature and glass cover temperature. An initial sensitivity analysis showed that the main variables of concern, that influences the optimality, are the concentration ratio, mass flow, tube diameter and saturation temperature (or operating pressure). Variables such as wind velocity and glass cover clearance will affect the entropy generation, but will have low to minimal effect on the minima. The convection on the outer tube is primarily assumed to be forced, in the form of wind. The effects of natural convection on the losses and optimization were not investigated. The model is theoretical and attempts to investigate the influence of entropy generation by fluid friction compared to entropy generation due to finite temperature differences. Generally a small scale scenario was investigated. Therefore, for the cases investigated, the turbine work output will be in the range of 50 to 350 kW.

2. Model and Mathematical Formulation

2.1. Model

The model is based on one-dimensional heat transfer through the receiver as shown in Figure 1. It is recognized that there will be temperature differences in the cross section of the receiver especially in the superheated section. This is not, however, taken into account since the superheated section is so much shorter compared to the two-phase and liquid region (cf. Table 1). There is forced convection on the inner tube perimeter that will transfer heat from the hot tube to the working fluid. The heat transfer coefficient on the inner wall of the receiver tube is determined by accepted correlations for both the single-phase as well as the two-phase region. From the outer tube area some of the focused heat is re-radiated to the glass cover. It is assumed that the vacuum is perfectly maintained at all times and the only heat transfer that takes place from the outer receiver tube to the inner glass cover is by means of radiation. Conduction takes place through the glass cover. The outer glass cover can be subject to forced convection (if wind is present) or natural convection (if no wind is present). For this study it was taken as the former with an assumed wind speed of 2 m/s. Furthermore the outer glass cover will also radiate heat to the atmosphere. The receiver tube is separated into three regions namely the liquid region, the two phase region and the superheated region as shown in Figure 2. Each of these regions will have different effects on the entropy generation.

2.2. Mathematical Formulation

2.2.1. Heat Transfer Coefficients - Single-Phase Region

For the single phase regions the Gnielinsky correlation is used to estimate the Nusselt number [14]:

$$Nu = \frac{(f/8)(Re - 1000)Pr}{1 + 12.7(f/8)^{1/2}(Pr^{2/3} - 1)} \tag{1}$$

In conjunction with the Gnielinsky equation, the first Petukhov equation for smooth tubes is used to obtain the friction factor [15]:

$$f = (0.79 \ln Re - 1.76)^{-2} \tag{2}$$

Once the Nusselt number is known the heat transfer coefficient can be obtained:

$$h = \left(\frac{k}{D}\right) Nu \tag{3}$$

The convection heat transfer from the inner tube wall to the working fluid is given by:

$$Q_{conv} = hA_{ri}\left(T_{ri} - T_{fluid}\right) \tag{4}$$

2.2.2. Heat Transfer Coefficients - Two-Phase Region

To obtain the two-phase heat transfer coefficient the procedures as described by Wojtan et al. [16,17] are used, which builds on the work of Kattan et al. [18] and Zürcher et al. [19]. The process for obtaining the two-phase heat transfer coefficient is quite involved and only the most important equations are stated here. The two-phase heat transfer coefficients can be calculated by combining the heat transfer coefficient for the wetted perimeter and the dry perimeter:

$$h_{tp} = \frac{\theta_{dry} h_{vapour} + \left(2\pi - \theta_{dry}\right) h_{wet}}{2\pi} \tag{5}$$

The wet heat transfer coefficient is determined by the nucleate boiling coefficient and the convective boiling coefficient:

$$h_{wet} = \left({h_{nb}}^3 + {h_{cb}}^3\right)^{1/3} \tag{6}$$

The vapour heat transfer coefficient can be determined by the following:

$$h_G = 0.023 \left[\frac{\dot{G} x D_{ri}}{\varepsilon_{void} \mu_G}\right]^{0.8} \left[\frac{k_G}{D_{ri}}\right] {Pr_G}^{0.4} \quad (7)$$

The dry angle (θ_{dry}) is dependent on the type of flow, for example slug, stratified, stratified-wavy (SW) or annular. At low mass velocities the flow will remain in the SW and Slug-SW zone, whereas if the mass velocity is large the flow will likely remain in the slug, intermittent and annular zones. It was seen from the numerical model that that Slug-SW and SW flow can cause a higher entropy generation due to less heat transfer and higher receiver temperatures. The second reason why SW and Slug-SW flow is not advantageous is that it may cause uneven heating of the tube wall. At high qualities dryout occurs before the flow moves into the misty zone. Dryout and misty zones are also characterized by lower heat transfer coefficients and higher temperatures. At lower pressure earlier transition to misty flow was also seen.

2.2.3. Conduction

The conduction through a cylinder wall (from the inner to the outer wall) is described by:

$$Q_{cond} = \frac{2\pi L k (T_i - T_o)}{\ln (D_o/D_i)} \quad (8)$$

Furthermore the thermal conductivity of the receiver was taken as that of steel 304L, and varies with temperature [5]:

$$k_r = 0.013 T_r + 15.2 \quad (9)$$

2.2.4. Heat Transfer Coefficients - Outer Surface

The forced convection coefficient for the outer surface of the glass cover was determined by making use of the Churchill and Bernstein correlation [20]:

$$Nu = 0.3 + \frac{0.62 Re^{1/2} Pr^{1/3}}{\left[1 + 0.4/Pr^{2/3}\right]^{1/4}} \left[1 + \left(\frac{Re}{28200}\right)^{5/8}\right]^{4/5} \quad (10)$$

which is valid for $RePr > 0.2$. The convection heat transfer from the outer glass tube to the surroundings is given by:

$$Q_{conv} = h A_{go} \left(T_{go} - T_{amb}\right) \quad (11)$$

The radiation from the outer glass tube to the atmosphere is given by:

$$Q_{rad} = A_{go} \sigma \varepsilon_g \left({T_{go}}^4 - {T_{sky}}^4\right) \quad (12)$$

Similar equations to what has been stated above have been used by Forristall[5] and Odeh et al.[4] The sky temperature was estimated at 8℃ below ambient [21]. An alternative equation is used by Garcia-Valladares and Velázquez [22]:

$${T_{sky}} = 0.0552 {T_{amb}}^{1.5} \quad (13)$$

A sensitivity analysis on the effective sky temperature showed minimal changes in results when Equation (13) was implemented (which can be calculated as approximately 4℃ if the ambient temperature is taken as 20℃). For the optimization and results the value of 8℃ for the effective sky was used.

2.2.5. Glass Cover Temperature

Radiation from the receiver to the glass cover is described by:

$$Q_{rad} = \frac{A_{ro} \sigma ({T_{ro}}^4 - {T_{gi}}^4)}{1/\varepsilon_r + \left(1 - \varepsilon_g/\varepsilon_g\right)(D_{ro}/D_{gi})} \quad (14\,a)$$

To determine the temperature of the glass cover, an energy balance can be performed around the cover:

$$Q_{rad,ro\rightarrow gi} = Q_{conv,go\rightarrow amb} + Q_{rad,go\rightarrow sky} \quad (14\,b)$$

The radiation through the vacuum, from the receiver to the glass must equal the radiation to the atmosphere from the outer surface as well as the convection losses from the outer surface due to the wind. Such an energy balance usually involves implicitly solving the glass temperatures.

2.2.6. Concentration Ratio

The optical efficiency is defined as the reflected solar energy (S_r) over the total solar irradiance (I_b), taken as 1000 W/m^2:

$$\eta_{opt} = \frac{S_r}{I_b}$$

The optical efficiency accounts for inefficiencies due to cover transmittance, absorptance, surface reflectivity and geometry. The optical efficiency was taken as 72%. The solar radiation falling on the receiver can be obtained by making use of the concentration ration (C_R):

$$q_{sun} = C_R S_r$$

$$Q_{sun} = q_{sun} A_s$$

The concentration ratio can also be determined from the trough width (W_a) and outer tube diameter (D_o):

$$C_R = \frac{W_a - D_{ro}}{\pi D_{ro}}$$

For a unit length the heat transfer area (A_s) is given by:

$$A_s = D_{ro}\pi$$

2.2.7. Pressure Losses

The single-phase pressure drop was obtained by:

$$\Delta P = f\left(\frac{L}{D_{ri}}\right)\frac{\rho V^2}{2} \quad (15)$$

The pressure drop in the two-phase region was determined by making use of the Friedel correlation which uses a two-phase flow multiplier in conjunction with a liquid pressure drop calculation [23,24]:

$$\Delta P_{tp} = \Delta P_L \phi^2 \quad (16)$$

where the liquid pressure drop is given by:

$$\Delta P_L = 4 f_L \dot{G}^2 \left(\frac{L}{D_{ri}}\right)\frac{1}{2\rho_L} \quad (17)$$

2.2.8. Second Law Analysis

The entropy generated by the finite temperature differences are determined by obtaining the destroyed exergy [21]. The exergy into the receiver is given as:

$$E_{in} = Q_{sun}\left(1 - \frac{T_{amb}}{T_{sun}}\right) \quad (18)$$

where T_{sun} in Equation (18) is the apparent sun temperature with a value of 4330 K [21]. The exergy into the working fluid is given by:

$$E_{out} = Q_{fluid}\left(1 - \frac{T_{amb}}{T_r}\right) \quad (19)$$

The destroyed exergy and entropy generation (due to finite temperature differences) is respectively given by:

$$E_{des} = E_{in} - E_{out} \quad (20)$$

$$S_{gen,dT} = \frac{E_{des}}{T_{amb}} \quad (21)$$

The entropy generation due to fluid friction can be obtained from [9]:

$$S_{gen,dP} = \left(\frac{\dot{m}}{\rho T_{in}}\right)\Delta P \quad (22)$$

A similar equation can be used for the two-phase region provided that the local specific volume is used [12]:

$$S_{gen,dP} = \left(\frac{\dot{m}v}{T_{in}}\right)\Delta P \quad (23)$$

3. Numerical Model and Optimisation

Water is heated from ambient conditions to a superheated state. This means the receiver is subject to both single phase-, as well as two-phase flow. Three regions must be solved: the liquid region, the two-phase region and the superheated region. As the receiver tube gets hotter lengthwise, more heat will be lost to the surroundings and changes in fluid properties will be perceived. Coolprop is used to estimate the fluid properties of air and water accurately [25]. A first law analysis is conducted on each unit section in the single-phase region. The fluid inlet temperature is known from a previous iterative step (cf. Figure 3). Subsequently, the fluid outlet, receiver and cover temperatures are then solved to ultimately estimate the heat losses and exergy destruction for that unit section (single-phase). For the two-phase region the length needed for a 2% quality change is iteratively calculated. As before (with the single phase region), the quantity of importance is the heat loss. The heat losses are estimated by obtaining the receiver and cover temperature. This process is explained in more detail in the following section. All entropy generation is solved by implementation of Equations 1 to 23 (as stated in section 2) in Python [26]. SciPy [27] packages are used in conjunction with Python for optimisation purposes. Note that the single-phase regions are handled slightly differently than the two-phase region. For the single phase regions each section is taken as a unit length, whereas for the two-phase region, the section length is determined by the length needed for a 2% quality change.

Other limitations of the model include that the heat losses through the bellows and structure are not taken into account. Furthermore, momentum and static pressure losses are not taken into account either. The model is mainly theoretical and the exact layout of the system is not taken into consideration. It is assumed that these losses will only effect the total entropy generation, but not the general trend of the cost function. This assumption is based on what was noted from the results where the total length for various operating pressures does not vary much for a specific mass flow. It can be seen from Table 1 that the total length needed for an operating pressure of 9 MPa is 17 metres longer than for 3 MPa.

Table 1: Length of regions for operating pressures 3, 5, 7 and 9 MPa for a mass flow of 0.15 kg/s and 0.4 kg/s respectively.

Mass flow = 0.15 kg/s					Mass flow = 0.4 kg/s			
Pressure (MPa)	**Liquid (m)**	**Two-Phase (m)**	**Vapour (m)**	**Total (m)**	**Liquid (m)**	**Two-Phase (m)**	**Vapour (m)**	**Total (m)**
3	71	143	12	226	190	384	32	606
5	83	134	16	233	222	360	42	624
7	92	126	20	238	247	337	53	637
9	100	118	25	243	268	315	64	647

Pressures lower than 3 MPa showed bad performance and the results for pressures lower than 3 MPa is not included in this paper. This phenomenon was due to longer two-phase regions for lower operating pressures and in some cases an earlier transition to the misty flow regimes (causing higher receiver temperatures and increasing heat losses). It can also be seen from the numerical model that slug and slug-SW (stratified-wavy) regimes cause lower heat transfer coefficients that could increase heat losses to a certain extent. Stratified flow regime was rarely triggered in the analysis since the Reynolds number would generally be out of range for the liquid region indicating that the flow was laminar.

3.2. Initial Parameters and Saturation Values

Table 2 lists the initial parameters that was used as input to the numerical model. A sensitivity analysis showed that the glass emissivities and effective sky temperature had minimal effects on the numerical results. It was also seen is that an increase in wind velocity would increase the entropy generation, but would not affect the maxima or minima. The same tendency can be seen if the receiver glass clearance is increased.

Table 2: Summary of fixed parameters used in the numerical model.

Parameter	Value
Glass emissivity (ε_g)	0.87
Receiver emissivity (ε_r)	0.92
Glass thermal conductivity (k_g)	1.05 W/m.K
Ambient temperature (T_{amb})	20℃
Effective sky temperature (T_{sky})	12℃
Solar irradiance (I)	1000 W/m^2
Optical efficiency (η_{opt})	0.72
Wind velocity (V_{wind})	2 m/s
Glass clearance	0.01 m
Tube thickness	0.002 m

From Table 3 it can be seen that the saturation temperature increases for higher operating pressures. The enthalpy of evaporation on the other hand decreases as the operating pressure increases. Due to this phenomenon the two-phase regions are also shorter for higher operating pressures. This is advantageous when considering the pressure drop over the two-phase length. For higher operating pressures the single-phase region, especially the liquid region, however tends to be much longer since longer receiver tube lengths are needed to reach the

saturation temperature. However, the entropy generation due to fluid friction in the liquid regions tends to be negligible when compared to the entropy generation (of both fluid friction and temperature differences) in the two-phase and superheated region.

Table 3: Operating pressure and corresponding saturation temperature, turbine inlet temperature and enthalpy of evaporation.

Operating pressure (MPa)	Saturation temperature (℃)	Turbine inlet temperature (℃)	Enthalpy of evaporation (kJ/kg)
3	233.9	280.7	1795.7
4	250.4	300.5	1714.1
5	264.0	316.8	1640.1
6	275.6	3308	1571.0
7	285.9	343.1	1505.0
8	295.1	354.1	1441.3
9	303.3	364.0	1379.1

3.3. Iterative Procedure

Figure 3 shows the iterative procedure followed during the numerical analysis to solve one section in the two-phase or single-phase region. In the single-phase region (liquid and superheated region) the relevant temperatures are solved for a unit section, while the section length in the two-phase region is determined by the length needed for a 2% quality change. The 2% quality change is adequate enough to capture the temperature changes since the receiver temperature (in the two-phase region) does not fluctuate greatly (cf. Figure 6). The heat transfer coefficient for the two-phase region is very large for the majority of cases. High heat transfer coefficients in the two-phase region will result in receiver temperatures close to saturation. Note that Figure 3 only shows the iterative procedure involved for one section. Solving the entire region involves determining the temperatures and entropy generation for each section before the total for the entire region can be obtained by summation. The turbine inlet temperature was taken as 20% higher than the saturation temperature. This was done to ensure fairly dry steam at the end of the expansion process. Note, however, this will still be dependent on the operating pressure under investigation.

3.3.1. Single-Phase Region

The entropy generation is obtained by first solving the relevant temperatures such as the fluid outlet temperature, the receiver temperature and the glass temperature. The outlet temperature is used as the inlet temperature for the next section after convergence is achieved. To solve the receiver temperature, the internal heat transfer coefficient must be obtained. As soon as the receiver temperature is estimated, an energy balance over the glass cover is used to obtain the glass inner and outer temperatures iteratively. The *'fmin'* function in SciPy is used to minimize the error involved with the energy balance over the cover. A new estimation of the heat into the unit length can be determined as soon as the losses are known. This value is compared with the value from a previous iteration and if the tolerance criteria ($\left|Q_{in} - Q_{in,new}\right| < 1\ Watt$) is satisfied the new value is accepted and all the temperatures are regarded as reasonably accurate. This procedure is continued until the saturation temperature (in the liquid region) or turbine inlet temperature (in the superheated region) is reached.

Figure 4 (a) depicts the temperature changes throughout the liquid region for a specific case where the mass flow rate, diameters and operating pressure is fixed. Figure 4 (b) depicts the heat losses from the receiver. It can be seen that the receiver temperature remains slightly

higher than the fluid temperature. Higher receiver temperatures will result in higher cover temperatures and more losses. The heat losses reach approximately 275 W (per unit section) at saturation temperature. This is fairly significant when keeping in mind that the maximum amount of focused heat per unit section is 2 kW (Q_{sun}). For higher saturation temperatures the losses become even more significant. It is also evident from Figure 4 (b) that the radiation losses are more significant for the first 5 sections. This is because the effective sky temperature is much lower than the cover temperature at this point. The convection losses are low at the start when the cover is still close to ambient temperature. However, the convection losses quickly exceed the radiation losses and contribute more to the total heat loss for the predominant part of the region. This is primarily due to a significant heat transfer coefficient on the outer surface of the vacuum cover. Both the convection losses as well as the radiation losses are highly dependent on the glass cover temperature.

A similar graph is shown for the superheated region in Figure 5 (a) and (b). It is noted that the superheated region (length of 19 m) is much shorter than the liquid region (length of 104 m). However, pressure drops through the superheated region are much higher than pressure drops through longer liquid regions. From Figures 4 and 5 it can also be seen that the glass temperature remains much lower than the receiver temperature. This is a good indication of the importance of the vacuum cover in minimizing the heat losses.

3.3.2. Two-Phase Region

The two-phase region is solved slightly differently to the single-phase region. The total heat needed for evaporation is given by:

$$Q = \dot{m} h_{fg} \tag{24a}$$

By estimating the heat into the receiver, the length needed for a 2% quality change can be determined:

$$L = \frac{Q_{2\%\ quality\ change}}{Q_{in\ per\ unit\ length}} \tag{24b}$$

The internal heat transfer coefficient of this section is then determined and the same procedures, as used for the single-phase regions, are followed. This procedure continues until a quality close to saturation is reached. The numerical code for the two phase section is validated by making use of data obtained from Wojtan et al. [17] in Figure 6 which shows how the heat transfer coefficient for R22 varies for the quality range.

Figure 7 shows the heat transfer coefficient variation for the quality range for water at a saturation temperature of 250.4 °C. At a quality of approximately 93 % the tube is subject to dryout and the heat transfer coefficient drops rapidly. This drop causes a spike in the receiver and glass temperatures as can be seen in Figure 8. Figure 8 shows the temperature of the working fluid, receiver and cover for the saturation temperature and parameters as used in Figure 7. For higher values of the two-phase heat transfer coefficient the receiver tube temperature will be closer to the saturation temperature. Furthermore, it was noted from the numerical model that misty, slug-SW and SW zones yielded lower heat transfer coefficients and higher receiver temperatures and thus more entropy generation in the two-phase region.

3.4. Optimization

From an initial investigation it was seen that the entropy generation is strongly influenced by the concentration ratio (C_R). If the concentration ratio was high, shorter lengths could be achieved. The concentration ratio influences the maximum heat that can be focused on the

receiver. There is however a limit to what can realistically be achieved with trough technology. For this research the maximum concentration ratio was taken as 45.

The optimization involved the minimization of the entropy generation for all three regions (liquid, two-phase and superheated). Due to the numerical nature of the analysis it was seen that the function evaluations tend to fluctuate slightly, causing multiple peaks and valleys.

Due to this, a simulated annealing algorithm (available in SciPy), is implemented to obtain an approximate optimum. The algorithm is based on the process of annealing molten metal and uses no gradient information. This process of cooling metal, such that a proper crystalline structure is achieved, is known as annealing and is analogous to attaining a minimum function value in the design space. Simulated annealing, is in part, random and two simulations with the exact same initial conditions and settings will not necessarily yield the exact same result.

4. Results and Discussion

Figure 9 depicts the entropy generation variation for various receiver tube diameters and operating pressures if the heat flux (Q_{sun}) remains constant at 2 kW/m. The entropy generation due to finite temperature differences ($S_{gen,dT}$) increases more or less linearly as the diameter increases. This is mainly due to an increase in exposed heat transfer area. Figure 9 (a) shows the result for a low mass flow rate case where $\dot{m} = 0.15\ kg/s$ and Figure 9 (b) for a high mass flow rate case where $\dot{m} = 0.4\ kg/s$. Comparing Figures 9 (a) and (b) it can be seen that increasing the mass flow rate will proportionally increase the entropy generation due to finite temperature difference. Note that this is not the case for the entropy generation due to fluid friction ($S_{gen,dP}$).

Figure 10 shows the change in entropy generation due to fluid friction for different cases. Figure 10 (a) is for a low mass flow case whereas Figure 10(b) is for a high mass flow case. Smaller diameters will significantly increase the entropy due to friction. This is especially true for the higher mass flow case and low operating pressure. Increasing the operating pressure will have the effect of lowering the entropy generation due to friction. This is due to the shorter two-phase regions for higher operating pressures as well as smaller pressure drops in the superheated region (due to higher vapour densities). The liquid regions are often longer for higher operating pressures but the entropy generation due to fluid friction in this region is small when compared to the other regions. Decreasing the diameter has the effect of quadratically increasing the entropy generation due to friction.

Figure 11 depicts the total entropy generation (combined $S_{gen,dT}$ and $S_{gen,dP}$). It can be seen from Figure 11 (a) (for a low mass flow case) that the entropy generation due to friction has a slight influence on the lowest operating pressure, 3MPa. The influence of fluid friction is seen more readily in Figure 11 (b) which is for the high mass flow case. For a high mass flow case the 3MPa operating pressure is highly influenced by $S_{gen,dP}$ at diameters 15 mm and 20 mm. The reason for a total entropy generation above 3000 W/K for the 15 mm case is that even though the heat losses are small the fluid friction is significant. The 5 MPa operating pressure is also heavily influenced by the fluid friction component ($S_{gen,dP}$) at a small tube diameter of 15 mm. The highest operating pressure shown, 9 MPa, is only slightly influenced by the fluid friction even when the tube diameter is small.

From Figures 9, 10 and 11 it can be seen that cases with higher operating pressures, smaller mass flow rates and larger diameters will primarily be subject to losses from temperature differences while cases with lower operating pressures, high mass flow rates and small diameters will be subject to losses from fluid friction.

Figures 12, 13, 14 and 15 depicts entropy generation contour plots for 4 different cases. Figure 12 is for the case of a low operating pressure and a low mass flow, Figure 13 for a high operating pressure and low mass flow and Figures 14 and 15 for the high mass flow scenario. For the contour plots (Figures 12,13,14 and 15) the heat flux was not fixed (as was done in Figures 8,9 and 10) but varied. The heat flux will depend on the concentration ratio (C_R). For higher concentration ratios, higher heat fluxes can be achieved. Higher concentration ratios are beneficial since more heat can be focused on a unit area when compared to lower concentration ratios. Also depicted on the contour plots are the constraint lines for 3 different concentration ratios: $C_R = 40$, $C_R = 45$ and $C_R = 50$. This is shown to clearly indicate that for higher concentration ratios one can move closer to the optimum region.

Figure 12 shows the contour plot for a low operating pressure of 3 MPa and a low mass flow rate of 0.15 kg/s. The increase in entropy generation at diameters smaller than 15 mm can be attributed to a large $S_{gen,dP}$ contribution while the lesser increases in entropy generation beyond a tube diameter of 20 mm can be attributed to $S_{gen,dT}$. The feasible region is located below the constraint lines to the left and can be represented as follows for a concentration ratio of 45:

$$C_R \leq 45 \tag{25a}$$

$$g(X) - 45 \leq 0 \tag{25b}$$

From Figure 12 it can be seen that diameters smaller than 15 mm tend to be highly influenced by $S_{gen,dP}$. This is due to the fluid friction component being more prevalent for smaller diameters. The optimum is located at the upper left region where Q_{sun} is at a maximum and the diameter remains small (but larger than 15 mm) to minimize losses to ambient. Beyond 20 mm the total entropy generation is mostly influenced by $S_{gen,dT}$. Increasing the diameter as well as the maximum amount of focused heat per unit section (Q_{sun}), will always have the effect of decreasing the entropy generation. This is due to the constraint lines having a steeper gradient than the contour plot lines that signify the $S_{gen,dT}$ contribution. It is however impractical to increase the receiver diameter and concentration ratio indefinitely simply to decrease the entropy generation. When taking the constraint into account, good design choices are located at $D_i = 20$ mm and $Q_{sun} \approx 2$ kW/m. Larger diameters such as 35 mm will require a Q_{sun} of around 3.5 kW/m.

Figure 13 shows the contour plot for a high operating pressure of 9 MPa and low mass flow rate of 0.15 kg/s. From this result it can be seen that the entropy generation in the design space is exclusively influenced by $S_{gen,dT}$, even for diameters smaller than 15 mm. Furthermore, the entropy generation is in the same order of magnitude as for Figure 11 due to similar mass flow rates.

Figure 14 shows the contour plot for a low operating pressure of 3 MPa and a high mass flow rate of 0.4 kg/s. In general the total entropy generation is larger than it is for lower mass flow rates (Figures 11 and 12) since the mass flow rate is proportional to the entropy generation. For diameters smaller than 15 mm the entropy generation increases drastically. This is due to $S_{gen,dP}$ becoming excessive for high mass flow rates, low operating pressures and small

diameters. For the case of a high mass flow and low operating pressure it can be seen that a diameter of 25 mm and $Q_{sun} = 2.5$ kW/m would be an adequate design.

Figure 15 shows the contour plot for a high operating pressure of 9 MPa and high mass flow rate of 0.4 kg/s. Once again (if the constraint is ignored) the optimum region is located in the upper left region were the inner tube diameter (D_i) is fairly small (15 mm) and Q_{sun} is at a maximum. When comparing Figure 14 (for a low operating pressure) and Figure 15 (for a high operating pressure) it can be seen that $S_{gen,dT}$ tends to be more dominant for the higher operating pressure. When increasing the diameter beyond 20 mm for an operating condition of 9 MPa the increase in $S_{gen,dT}$ is more significant than for 3 MPa. This is due to the $S_{gen,dT}$ component having a larger impact on the total entropy generation at high saturation temperatures. However, decreasing D_i beyond 15 mm (in the case of an operating pressure of 3 MPa) will increase the entropy generation drastically. This is due to the $S_{gen,dP}$ component becoming excessive for lower operating pressures, partly due to the longer two-phase regions as well as a larger two-phase flow multiplier for the lower operating pressures.

The simulated annealing results are shown in Table 4. The optimal operating pressure increases as the mass flow rate increases. It should however, also be recognised that higher mass flow rates will result in more available work. Ideally one would like a high work output, while still achieving low entropy generation rates.

Table 4: Simulated annealing optimization results: Optimum pressure for various mass flow rates with $D_i = 20$ mm.

Mass flow rate (kg/s)	Operating pressure (MPa)	Entropy generation (W/K)
0.15	3.597	903
0.2	3.815	1211
0.25	3.948	1523
0.3	4.680	1838
0.35	5.470	2156
0.4	6.715	2478

Table 5 shows the influence of the operating pressure on the work and total entropy generation for a mass flow rate of 0.4 kg/s and a constant diameter of 20 mm. An operating pressure of 6 MPa seems to yield the lowest total entropy generation. However, operating pressures 7, 8 and 9 MPa yield more work for slight increases in the total entropy generation and are also favourable. Pressures below 6 MPa yield less work and higher entropy generation and are therefore not as favourable.

Table 5: Total entropy generation and work output for operating pressures 3 to 9 MPa for a mass flow of 0.4 kg/s and inner tube diameter of 20 mm and a concentration ratio of 45.

Operating pressure (MPa)	Total Entropy Generation (W/K)	Work (kW)
3	2561.0	242.8
4	2511.6	263.2
5	2489.1	278.8
6	2478.3	291.2
7	2483.2	301.6
8	2485.5	310.3

9	2496.1	317.9

Figure 16 shows the change in entropy and work for various mass flow rates. Each point corresponds to an operating pressure. As the operating pressure is increased the maximum work that can be extracted also increases. At higher mass flow rates the curve is more rounded as the fluid friction component causes the total entropy generation to increase for low operating pressures (3 MPa) and high mass flow rates (0.4 kg/s). For lower mass flow rates (0.15 kg/s) the shape of the curve is more linear in form. This is due to the fluid friction component having less of an effect on the entropy generation at lower mass flow rates and lower operating pressures.

5. Conclusion

In this study a second law numerical analysis was conducted on a parabolic trough receiver tube that uses water as a working fluid. The main variables that were investigated included the operating pressure (or saturation temperature), the mass flow rate, the concentration ratio and tube diameter. Low operating pressures usually require longer two-phase regions due to a larger enthalpy of evaporation. This two-phase region can contribute significantly to the entropy generation due to fluid friction, especially at low operating pressures. For this reason operating pressures below 3 MPa are not recommended regardless of mass flow rate or receiver tube diameter.

Contributions from the entropy fluid friction component can be extreme for high mass flow rates and diameters smaller than 15 mm. In general, the fluid friction component becomes small when compared to the finite temperature difference component, for diameters larger than 20 mm. Increasing the receiver tube diameter will increase the entropy due to temperature differences if the maximum amount of focused heat (Q_{sun}) is kept constant. This is due to the increased exposed heat transfer surface. The heat flux (Q_{sun}) is determined by the concentration ratio and is limited to around 45 for 2D trough technology. On the other hand increasing receiver tube diameter as well as Q_{sun} will decrease the entropy generation, but this effect is only marginal for larger tube diameters.

It was also seen that the optimal operating pressure tends to increase if higher mass flow rates are considered. Higher operating pressures tend to have a more advantageous effect on the maximum work output while having a small to negligible effect on increasing the entropy generation.

Acknowledgements

We would like to thank the University of Pretoria, University of Stellenbosch, NRF, TESP, SANERI/SANEDI, CSIR, EEDSM hub and NAC for the funding during the course of this work.

References

[1] Eck M, Zarza E, Eickhoff M, Rheinländer J, Valenzuela, L. (2003) Applied research concerning the direct steam generation in parabolic troughs. Sol Energ 74:341-351.

[2] Price H, Lüpfert E, Kearney D, Zarza E, Cohen G, Gee R, Mohoney R (2002) Advances in parabolic trough solar technology. J Sol Energ Engineering 124:109-125.

[3] Liu QB, Wang YL, Gao ZC, Sui J, Jin HG, Li HP (2010) Experimental investigation on a parabolic trough solar collector for thermal power generation. Sci China Tech Sci 53: 52-56.

[4] Odeh S, Morrison G, Behnia M (1998) Modelling of parabolic trough direct steam generation solar collectors. Sol Energ 62:395-406.

[5] Forristall R. Heat transfer analysis and modelling of a parabolic trough solar receiver implemented in engineering equation solver. (2003) Technical Report; National Renewable Energy Laboratory.
[6] Roesle M, Coskun V, Steinfeld A (2011) Numerical analysis of heat loss from a parabolic trough absorber tube with active vacuum system. J Sol Engineering 133:1-5.
[7] Koroneos C, Spachos T, Moussiopoulos N (2003) Exergetic analysis of renewable energy sources. Renew Energ 28:295-310.
[8] Singh N, Kanshik S, Misra R (2000) Exergetic analysis of a solar thermal power systems. Renew Energ 19:135-143.
[9] Bejan A (1996) Entropy generation minimization: The method of thermodynamic optimization of finite size systems and finite time processes. CRC Press.
[10] Ratts E, Raut A (2004) Entropy generation minimisation of fully developed internal flow with constant heat flux. J Heat Tran 126:656-659.
[11] Sahin A (2000) Entropy generation in turbulent liquid flow through a smooth duct subjected to constant wall temperature. Int J Heat Mass Tran 43:1469-1478.
[12] Revellin R, Lips S, Khandehar S, Bonjour J (2009) Local entropy generation for saturated two-phase flow. Energy 34:1113-21.
[13] Barlev D, Vidu R, Stroewe P (2011) Innovations in concentrated solar power. Sol Energ Mat Sol C 95(27):3-25.
[14] Gnielinsky V (1976) New equations for heat and mass transfer in turbulent pipe and channel flow. Int Chem Eng 1(2):350-67.
[15] Petukhov B (1970) Heat transfer and friction in turbulent pipe flow with variable physical properties. Adv Heat Tran 6:503-64.
[16] Wojtan L, Ursenbacher T, Thome J (2005a) Investigation of flow boiling in horizontal tubes part 1: A new diabetic two-phase flow pattern map. Int J Heat Mass Tran 48:2955-69.
[17] Wojtan L, Ursenbacher T, Thome J (2005b) Investigation of flow boiling in horizontal tubes part 2: Development of a new heat transfer model for stratified-wavy, dryout and misty flow regimes. Int J Heat Mass Tran 48:2970-85.
[18] Kattan N, Thome JR, Favrat D (1998) Flow boiling in horizontal tubes: Part 1 - development of a diabatic two-phase flow pattern map. J Heat Tran 120:140-147.
[19] Zürcher O, Favrat D, Thome JR (2002) Evaporation of refrigerants in a horizontal tube: an improved flow patter dependent heat transfer model compared to ammonia data. Int J Heat Mass Tran 45:303-317.
[20] Churchill S, Bernstein M (1977) A correlating equation for forced convection from gases and liquids to a circular cylinder in cross-flow. J Heat Trans - T ASME C 99:300-6.
[21] Kalogirou S (2009) Solar energy engineering: Processes and systems. Elsevier Inc.
[22] Garcia-Valladares O, Velázquez N (2009) Numerical simulation of parabolic trough collector: Improvement using counterflow concentric circular heat exchangers. J Heat Mass Tran 52:597-609.

[23] Thome J (2004) Wolverine Tube Heat Transfer Data Book III. Wolverine Tube Inc; URL: http://www.wlv.com.
[24] Friedel F (1979) Improved friction pressure drop correlations for horizontal and vertical two-phase pipe flow. European two-phase flow group meeting. Ispra, Italy. Paper E2.
[25] Bell I. Coolprop (2013) URL: http://coolprop-sourceforge.net.
[26] Python Software Foundation . Python (2011) URL: http://www.python.org/doc/.
[27] Scipy Community . Scipy (2011) URL: http://docs.scipy.org/doc/.

List of Figures

Fig. 15 Contour plot for high mass flow rate of 0.4 kg/s and a high operating pressure of 10 MPa showing constraint lines due to concentration ratio.

Fig. 16 Influence of the operating pressure and mass flow rate on the work and entropy generation for a constant receiver tube diameter of 20 mm.

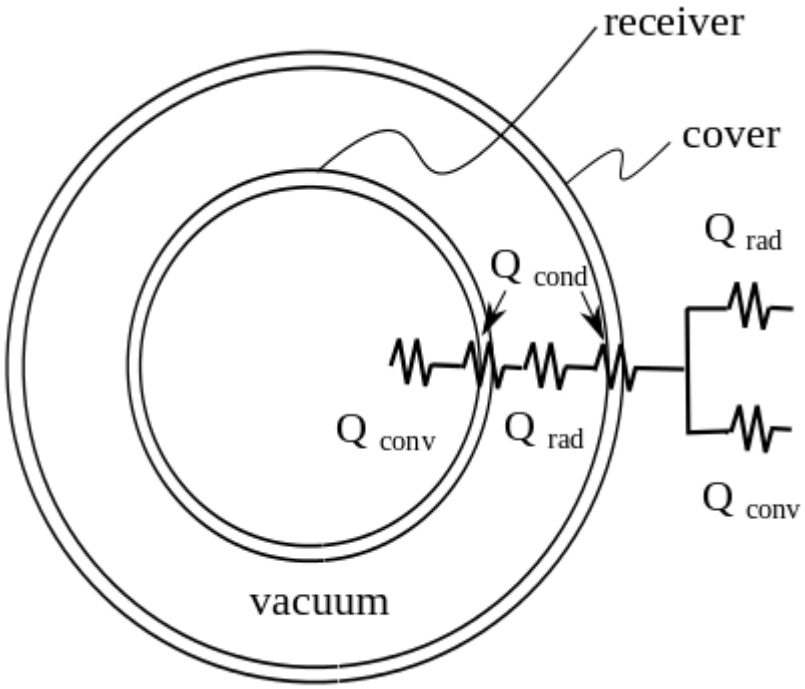

Fig. 1 One-dimensional heat transfer through the receiver assembly

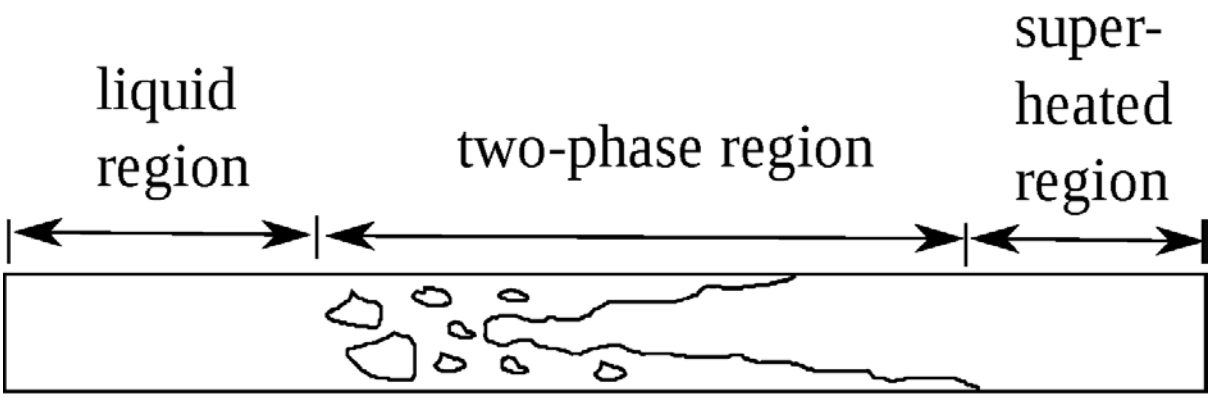

Fig. 2 Receiver tube regions

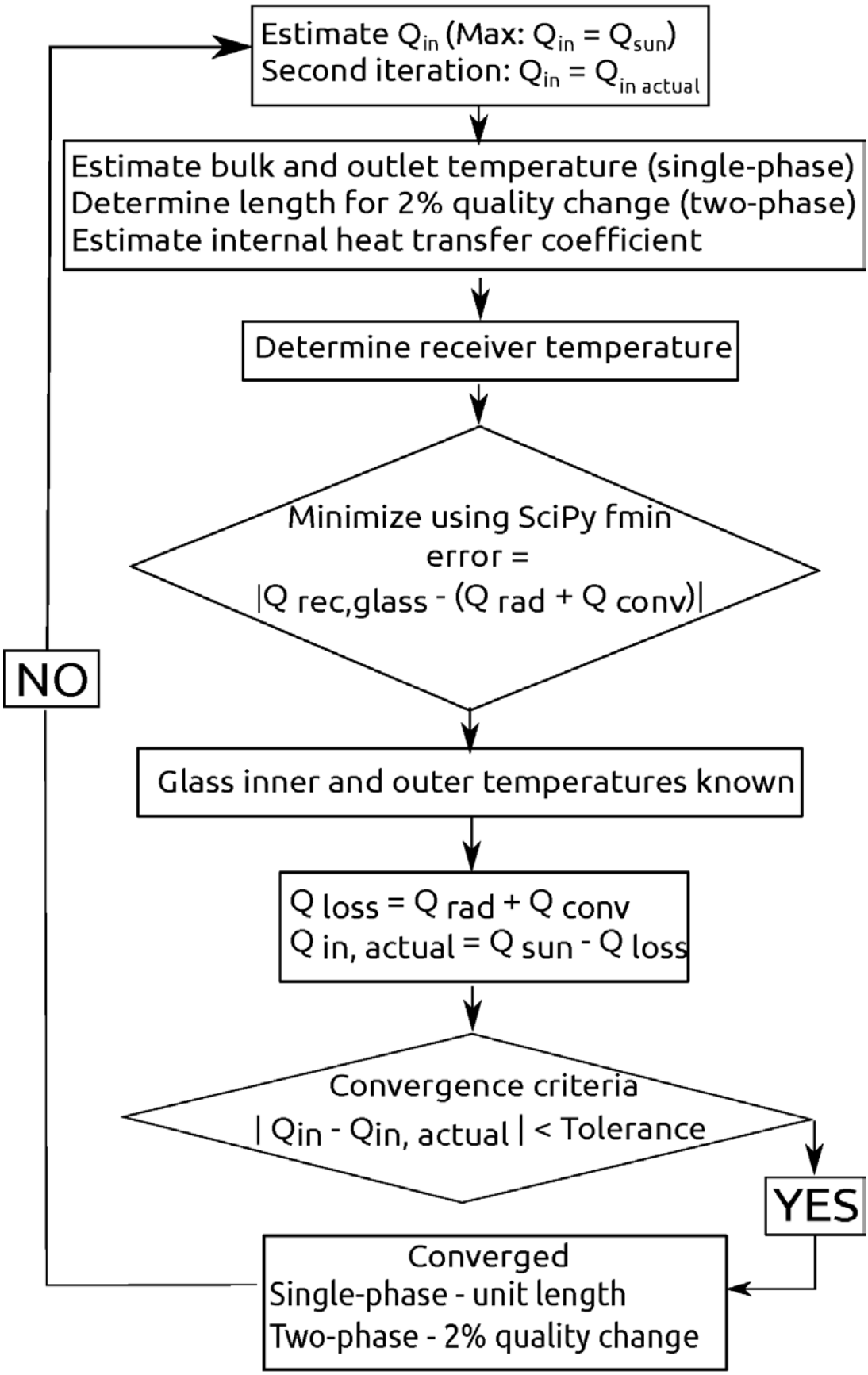

Fig. 3 Diagram showing the iterative procedure

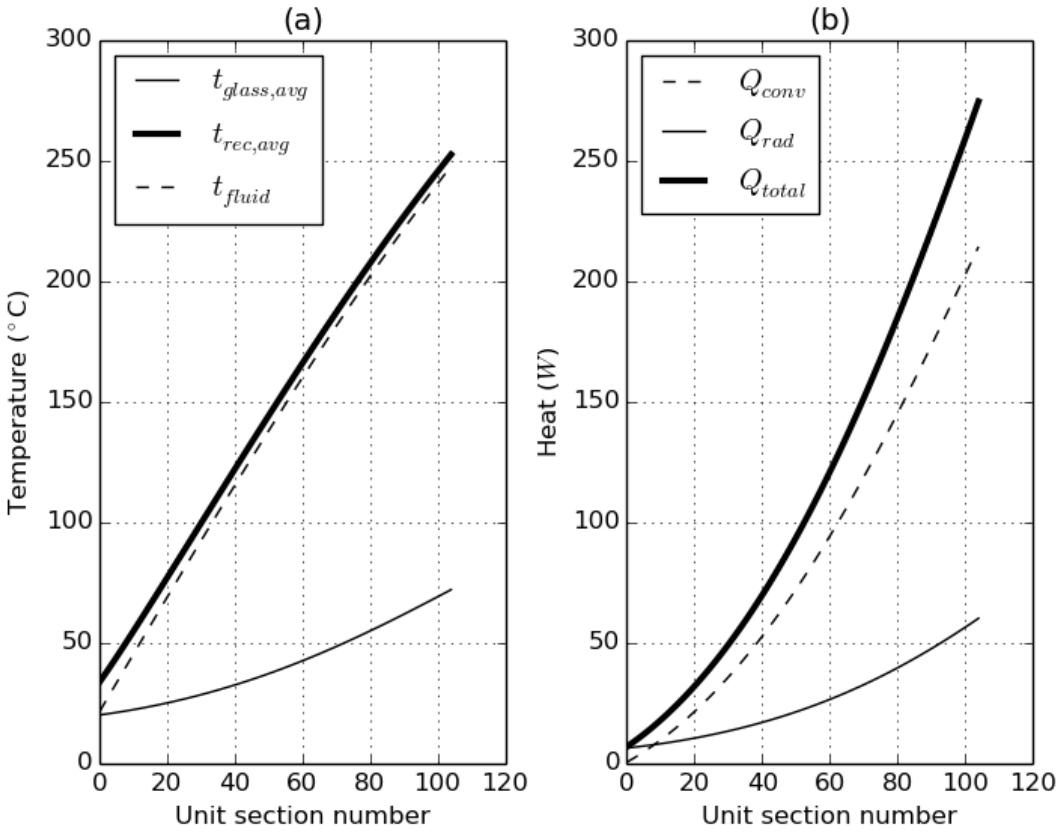

Fig. 4 Results of first law analysis for the liquid region for the case of T_{sat} = 250.4 °C (4 MPa), D_i = 25mm, Q_{sun} = 2 kW/m and a mass flow of 0.2 kg/s (a) Receiver, glass and fluid temperature (b) Heat losses

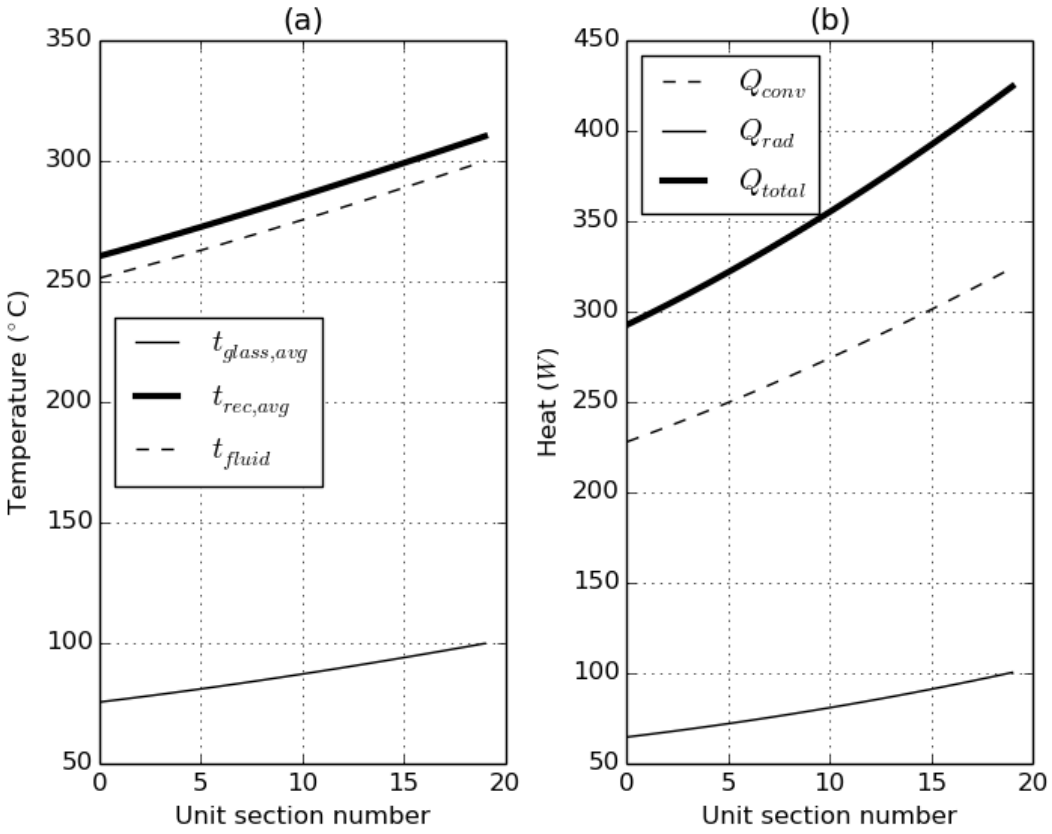

Fig. 5 Results of first law analysis for the superheated region for the case of T_{sat} = 250.4 °C (4 MPa), D_i = 25mm, Q_{sun} = 2 kW/m and a mass flow of 0.2 kg/s (a) Receiver, glass and fluid temperature (b) Heat losses

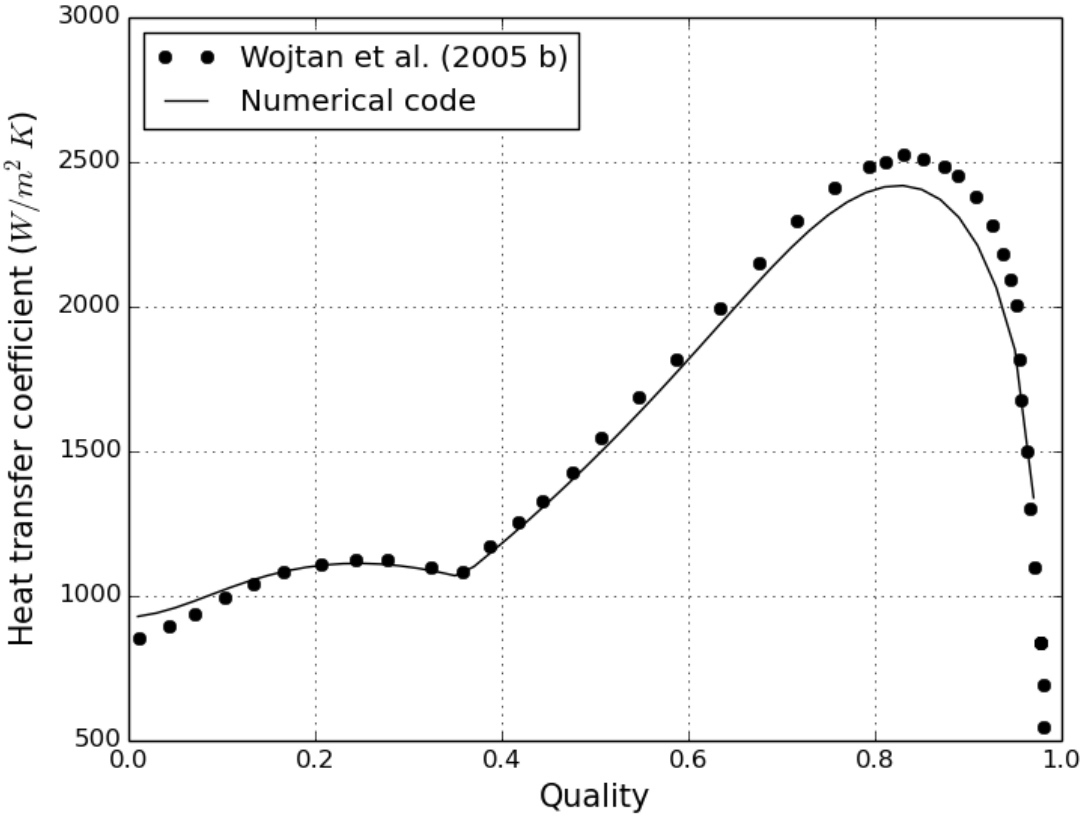

Fig. 6 Two-phase flow validation for R22 where $\dot{G}$= 150 kg/m^{2}s, D_i = 13.84 mm, T_{sat} = 5 °C and a heat flux of 3.6 kW/m^2

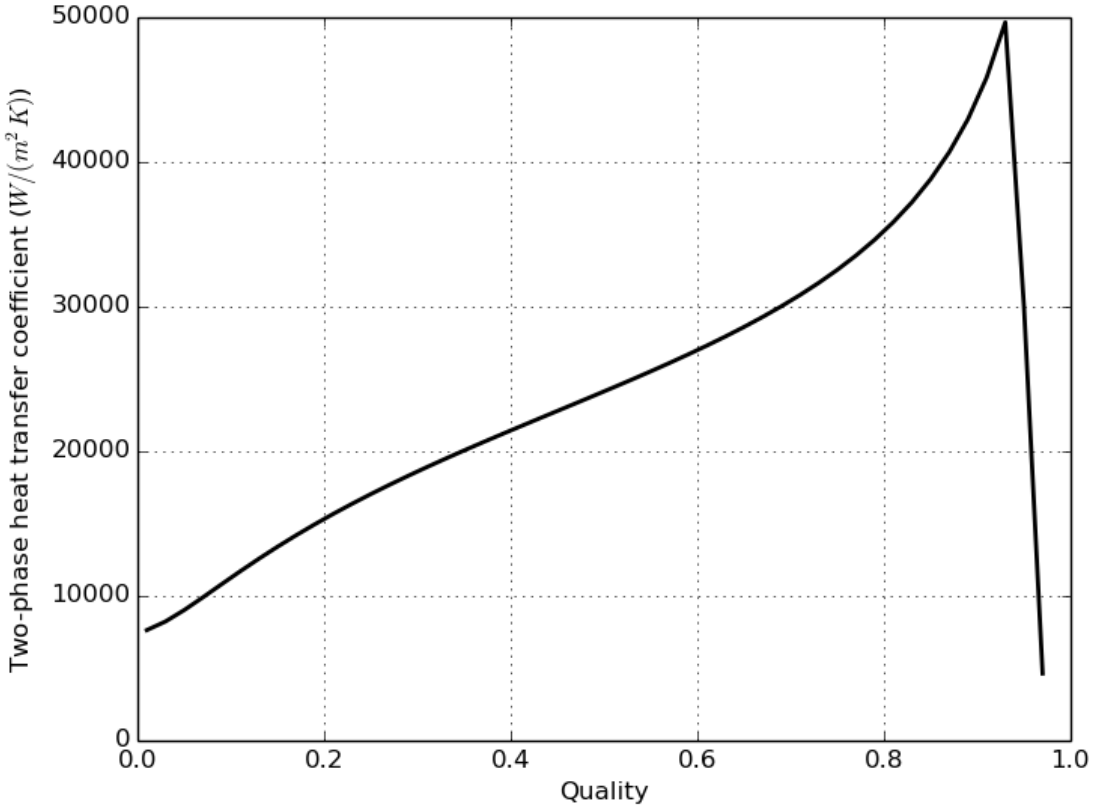

Fig. 7 Heat transfer coefficient for the two-phase region for the case of T_{sat} = 250.4 °C (4 MPa), D_i = 25mm, Q_{sun} = 2 kW/m and a mass flow of 0.2 kg/s

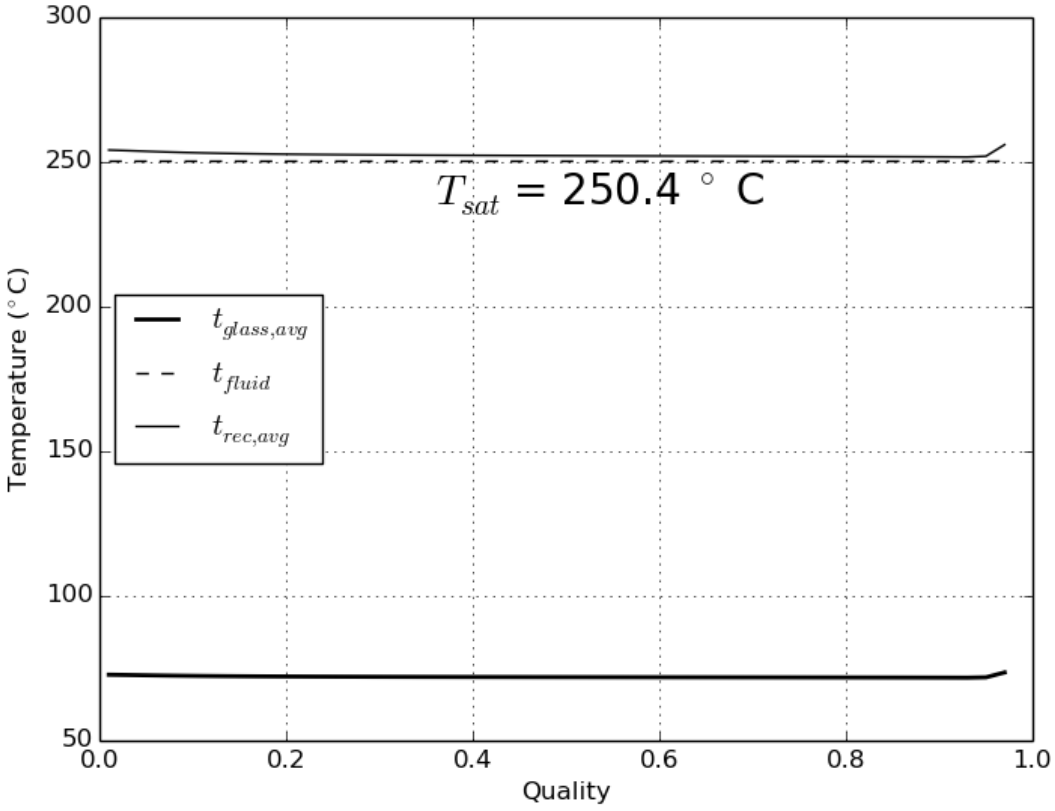

Fig. 8 Glass, fluid and receiver temperature for the two-phase region for the case of T_{sat} = 250.4 °C (4 MPa), D_i = 25mm, Q_{sun} = 2 kW/m and a mass flow of 0.2 kg/s

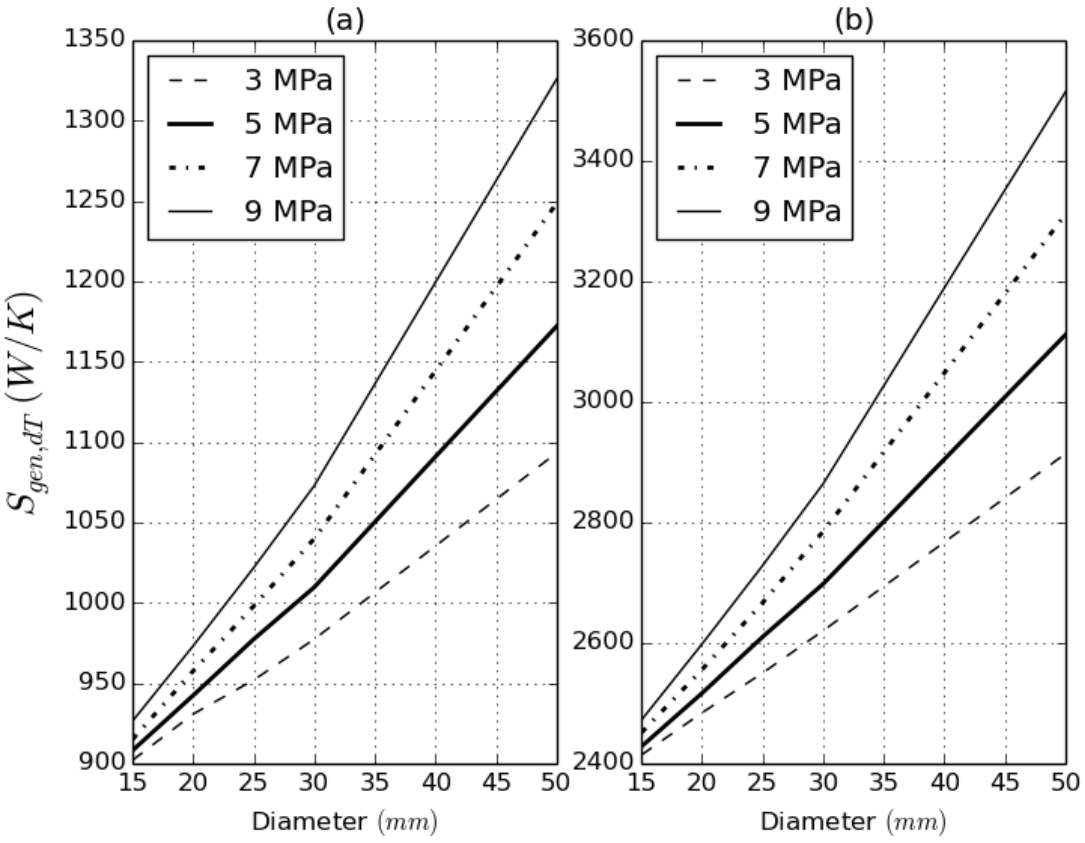

Fig. 9 Entropy generation due to finite temperature differences for various operating pressures and a constant heat flux of 2kW/m (a) Mass flow of 0.15 kg/s (b) Mass flow of 0.4 kg/s

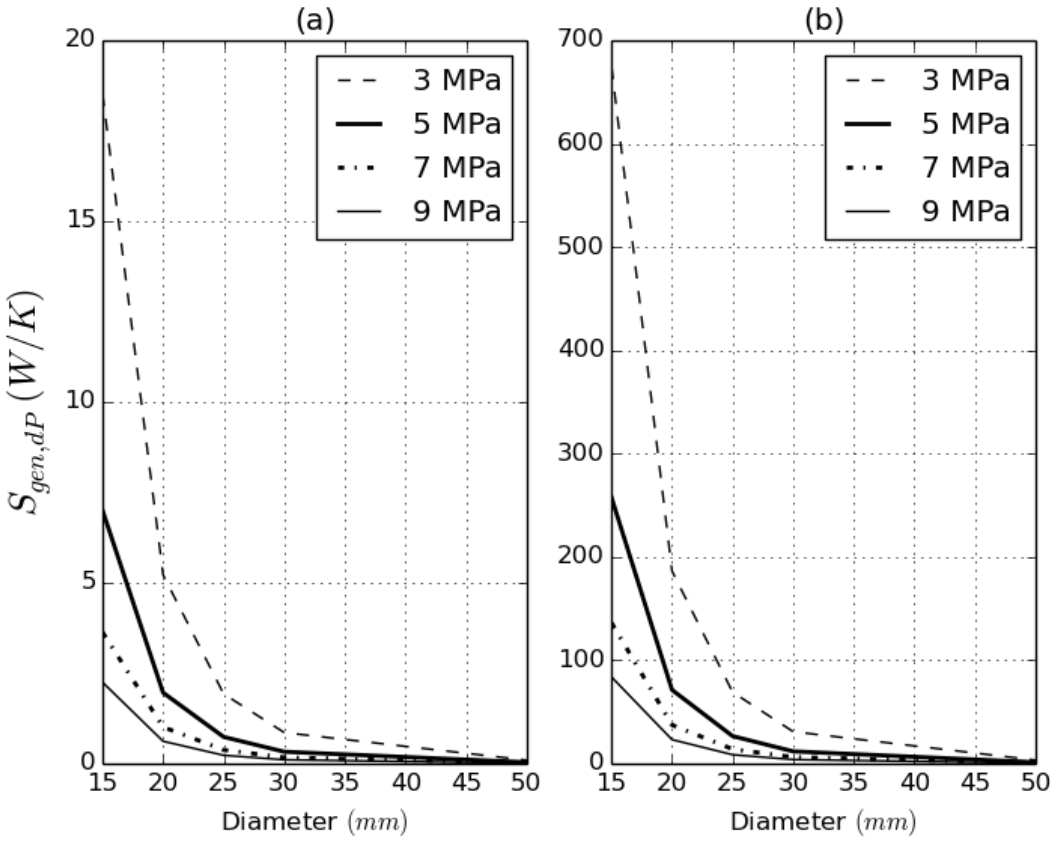

Fig. 10 Entropy generation due to fluid friction for various operating pressures and a constant heat flux of 2kW/m. (a) Mass flow of 0.15 kg/s (b) Mass flow of 0.4 kg/s

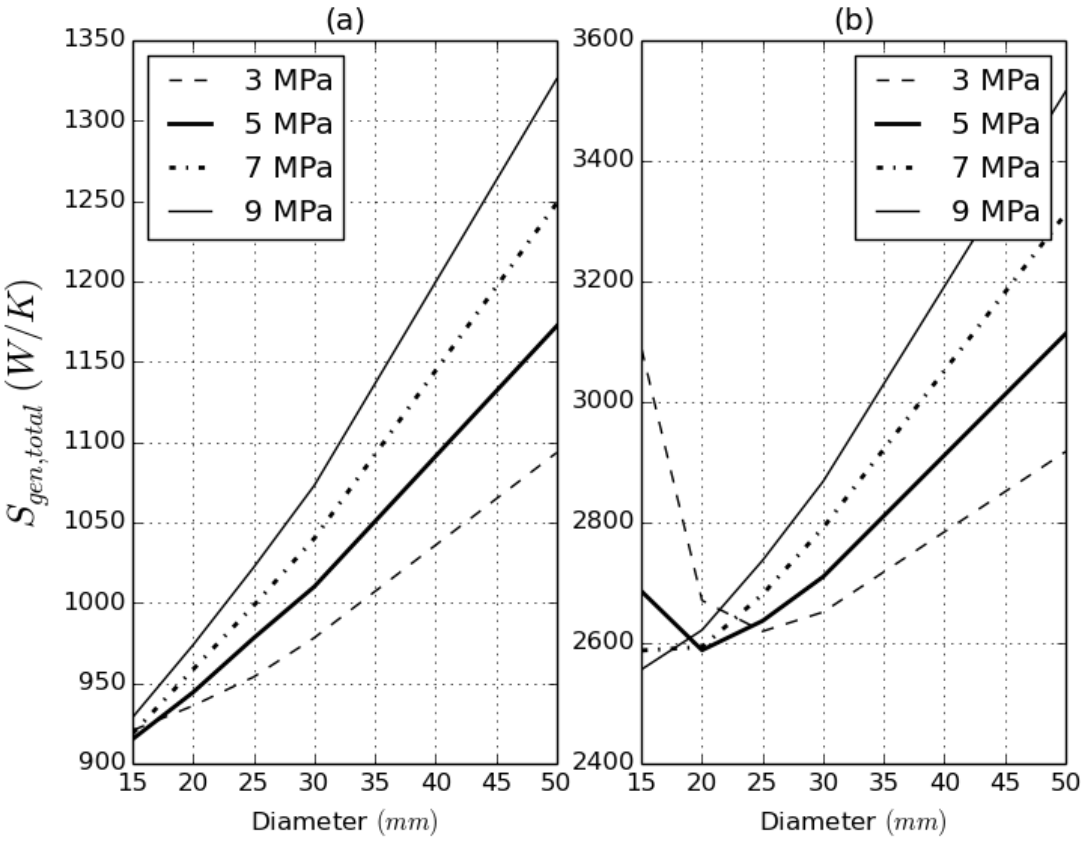

Fig. 11 Total entropy generation for various operating pressures and a constant heat flux of 2kW/m (a) Mass flow of 0.15 kg/s (b) Mass flow of 0.4 kg/s

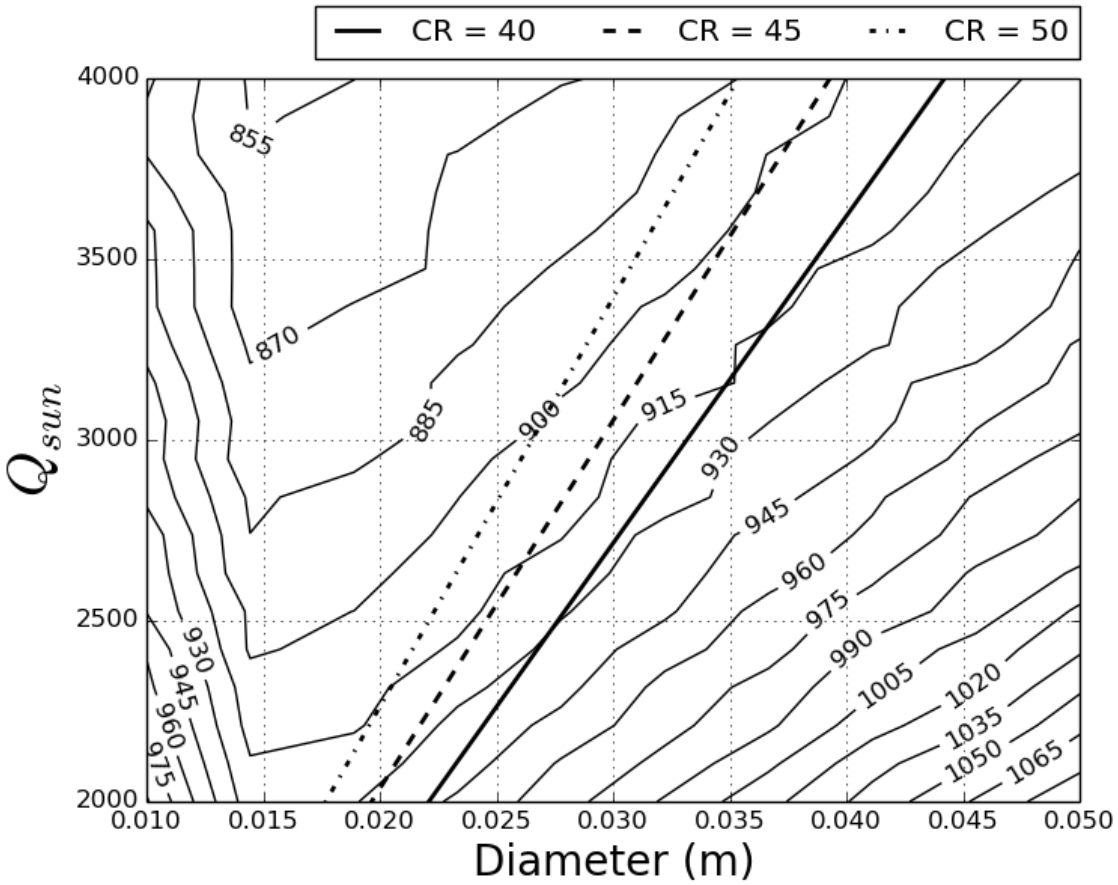

Fig. 12 Contour plot for low mass flow rate of 0.15 kg/s and a low operating pressure of 3 MPa and showing constraint lines due to concentration ratio

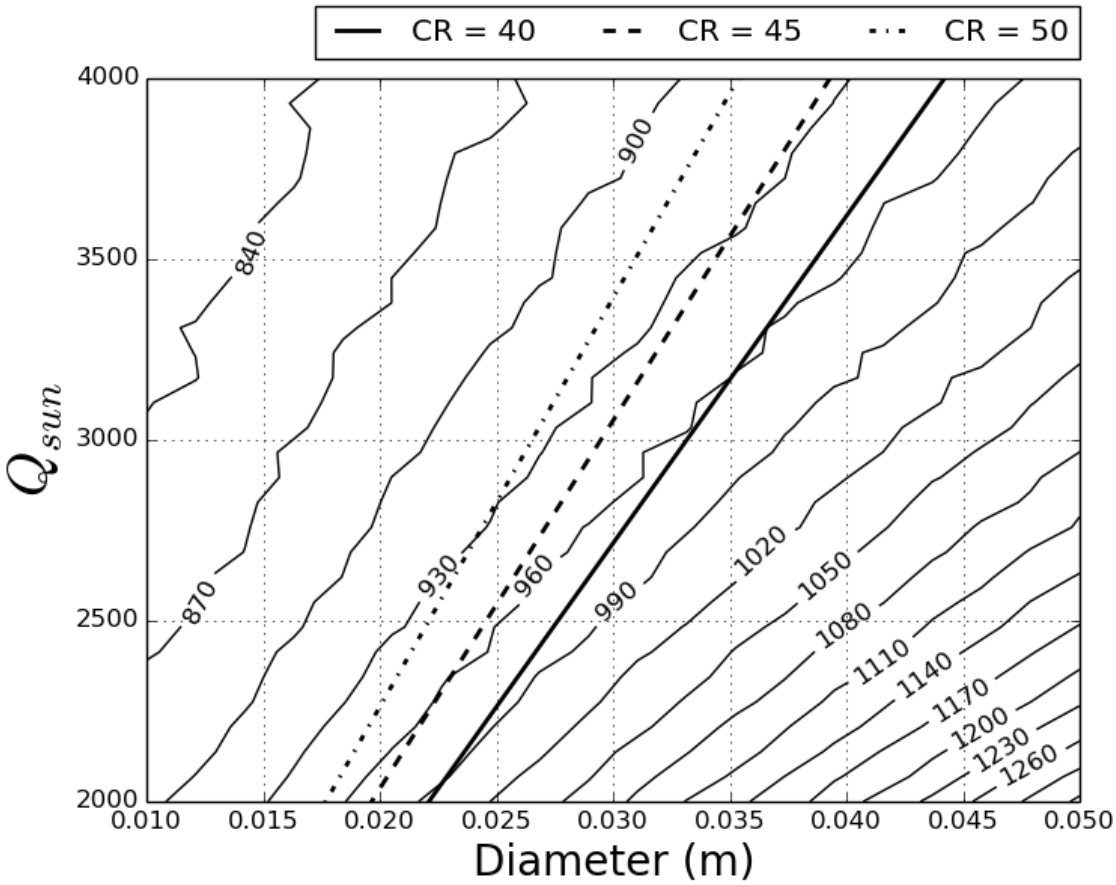

Fig. 13 Contour plot for low mass flow rate of 0.15 kg/s and a high operating pressure of 9 MPa and showing constraint lines due to concentration ratio

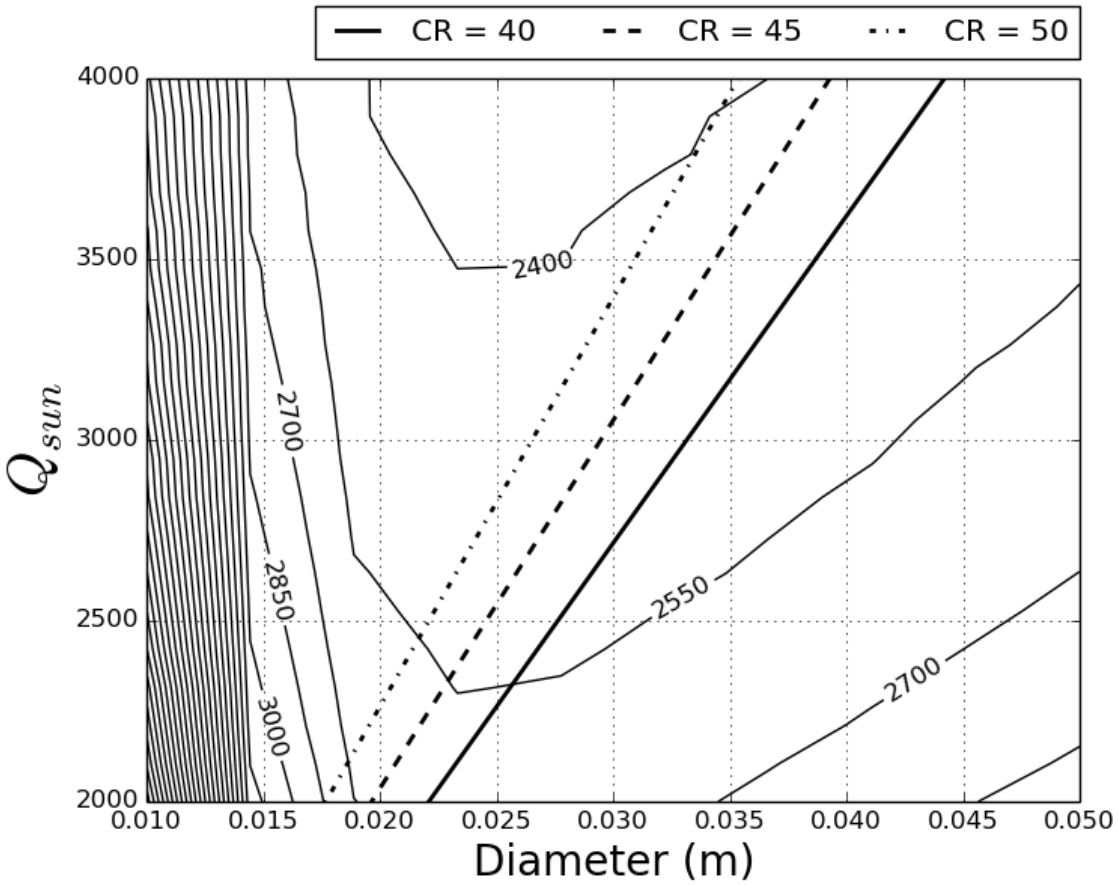

Fig. 14 Contour plot for high mass flow rate of 0.4 kg/s and a low operating pressure of 3 MPa and showing constraint lines due to concentration ratio

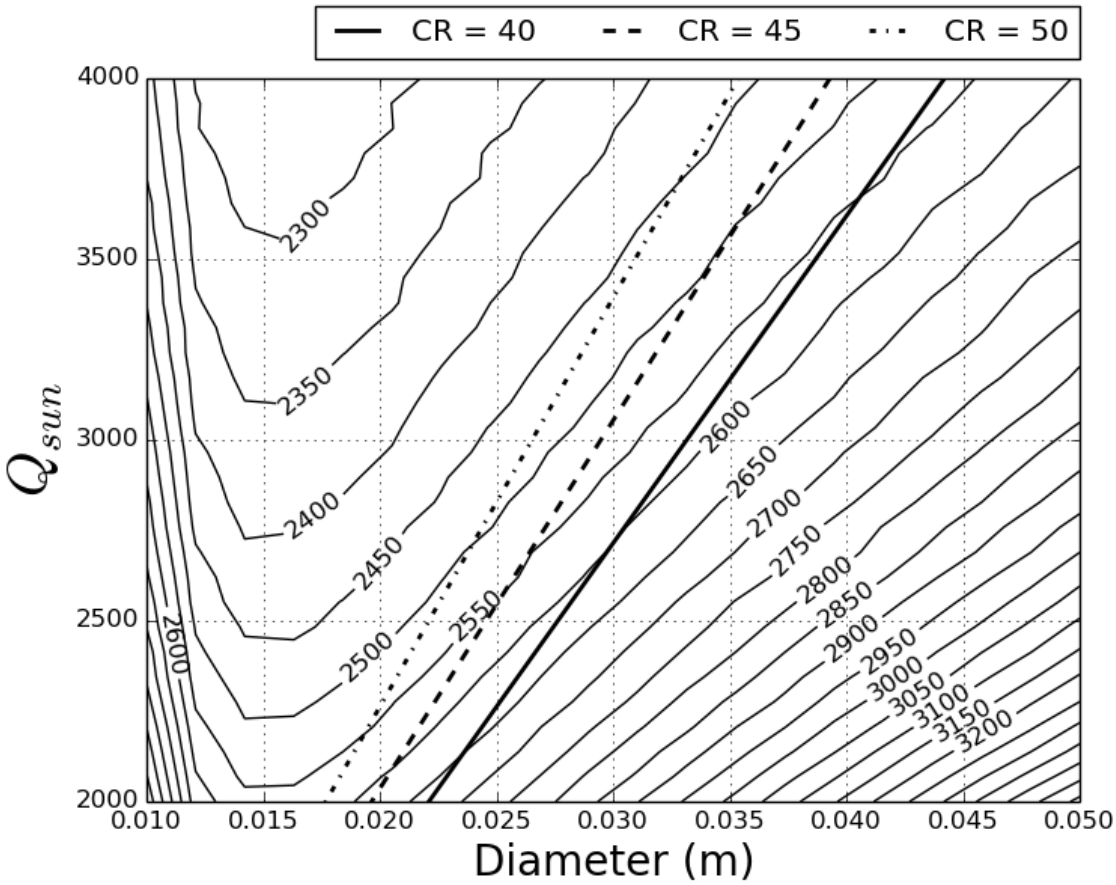

Fig. 15 Contour plot for high mass flow rate of 0.4 kg/s and a high operating pressure of 9 MPa and showing constraint lines due to concentration ratio

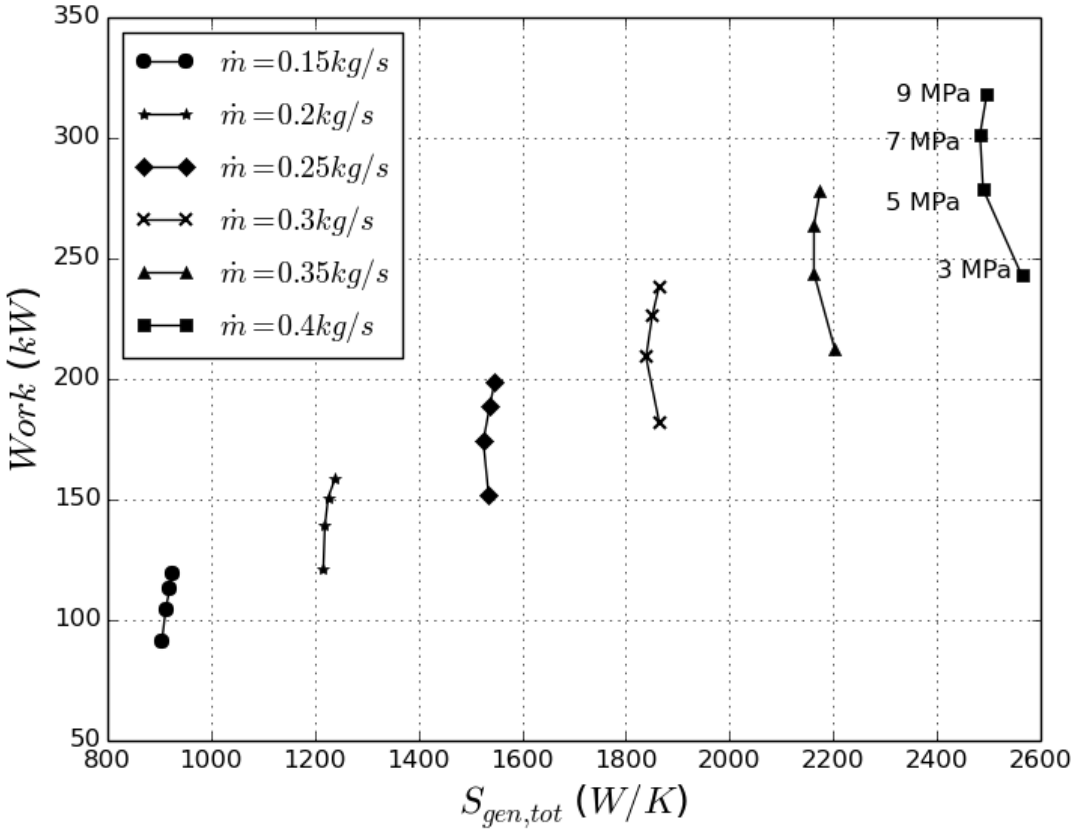

Fig 16: Influence of the operating pressure and mass flow rate on the work and entropy generation for a constant receiver tube inner diameter of 20 mm and concentration ratio of 45